Unsupervised Multitemporal Multiclass Change Detection

Rogério G. Negri*, Alejandro C. Frery *Senior Member, IEEE*, Wallace Casaca, Paolo Gamba *Fellow, IEEE*, Avik Bhattacharya *Senior Member, IEEE*

***Abstract*—We address the crucial task of identifying changes in land cover using remotely sensed imagery. While most change detection methods focus on two images, we introduce an unsupervised approach that considers long image series (more than two), supporting a more nuanced differentiation between changed and unchanged areas. The proposed technique transforms input data to a new representation, capturing the target's spectral response changes over time. Areas with minimal response variation are identified as non-changing and distinguished from regions that have undergone modifications. The method further categorizes, utilizing statistical procedures, regions undergoing spatiotemporal modifications into seasonal or permanent changes. Experimental validation using simulated and real-world remote sensing image series demonstrates the effectiveness of the proposed approach.**

***Index Terms*—Unsupervised; time series; change detection; feature extraction; statistical modeling.**

I. Introduction

With the rapid progress in Earth observation methods, acquiring remotely sensed imagery of specific areas at multiple time points has become increasingly convenient. In this context, identifying land cover and usage alterations is a fundamental and valuable task with applications spanning urban planning, damage assessment, deforestation, and landscape monitoring [1]. In this context, techniques for detecting spatiotemporal changes assume an essential role.

In the remote sensing literature, change detection refers to identifying alterations that have occurred in a specific location by analyzing images recorded in distinct times [2–4]. The most successful change detection techniques find their origins in principles derived from Pattern Recognition and Digital Image Processing. As outlined by Wu et al. [5], these techniques can be classified into (i) image algebra, (ii) image transformations, (iii) feature extraction, (iv) image classification, and (v) various other methods. More generically, these techniques may also grouped as statistical or artificial intelligence-based approaches.

Moreover, change detection approaches can be categorized into two distinct approaches: supervised and unsupervised [6]. While supervised methods demand labeled data for training, the unsupervised approach is autonomously guided through processes of clustering and thresholding. The fact that prior knowledge is not a prerequisite makes unsupervised methods particularly enticing compared to their supervised counterparts.

According to Liu et al. [7], change detection techniques can be classified based on their ultimate objective into binary and multiclass methods. The former treats all types of changes as a single change class, while the latter aims to identify different classes of changes. Typically, binary methods are defined within an unsupervised paradigm, while multiclass methods are associated with supervised approaches.

A plethora of alternatives for unsupervised change detection is found in the recent literature. Following a statistical-based approach, Hao et al. [8] used the Expectation-Maximization algorithm to estimate distributions for changed and non-changed areas, which are then integrated into the active contour model to map changes regarding a pair of images. Gong et al. [9] presented a change detection approach for bi-temporal synthetic aperture radar (SAR) images, where principal component analysis and Gabor filters are applied to separate irrelevant from relevant temporal changes. Conradsen et al. [10] proposed a likelihood ratio test statistic for assessing the homogeneity of complex variance-covariance matrices in a time series of polarimetric SAR (PolSAR) data, allowing to determine the time points of change and mapping the spatiotemporal changes. Nascimento et al. [11] proposed a technique based on generalized entropies under the complex Wishart model that can identify changes in fully PolSAR image sequences of arbitrary length. Zanetti and Bruzzone [12] presented a compound multiclass mixture model, broadening the statistical framework for change detection, allowing temporal correlation analysis, and identifying unchanged and changed pixels based on the bimodal behavior of the difference image's magnitude histogram. Zhang et al. [13] combined difference representation learning and unsupervised clustering into a unified model to learn Gaussian-distributed and discriminative difference representations for non-change and different types of changes. Chirakkal et al. [14] introduced a pixel-wise and sensor-independent fusion technique that exploits the Kronecker product concept to delineate the disparities between two images. Fonseca et al. [15] used wavelets and energy correlation screening concepts to formalize an unsupervised

This research was funded by the São Paulo Research Foundation (FAPESP), grants 2021/01305-6 and 2021/03328-3, and National Council for Scientific and Technological Development (CNPq), grants 305220/2022-5 and 316228/2021-4, and by the Faculty Strategic Research Grant 410695, Victoria University of Wellington.

R.G. Negri is with the Science and Technology Institute (ICT), São Paulo State University (UNESP), São José dos Campos, Brazil. A.C. Frery is with the School of Mathematics and Statistics, Victoria University of Wellington, New Zealand. W. Casaca is with the Institute of Biosciences, Letters and Exact Sciences (IBILCE), São Paulo State University (UNESP), São José do Rio Preto, Brazil. P. Gamba is with the Telecommunications and Remote Sensing Laboratory, Department of Electrical, Biomedical and Computer Engineering, Università di Pavia, Italy. A. Bhattacharyya is with the Centre of Studies in Resources Engineering (CSRE), Indian Institute of Technology Bombay, Mumbai, India.

*corresponding author: rogerio.negri@unesp.br

Manuscript received January, 2024; revised

method, known as WECS, for mapping the changes and non-changes regarding a period of interest.

Regarding artificial intelligent-based schemes, Wu et al. [5] utilized Slow Feature Analysis to extract information from multispectral image pairs and map temporal changes in an unsupervised manner. Li et al. [16] introduced a top-down cascade clustering technique for change detection, which involves log-ratio image generation and kernel K-Means clustering for mapping changes using pairs of SAR images. Huang et al. [17] showed a pairwise unsupervised change detection process guided by a two-component version of the Otsu threshold parametrized by the Firefly meta-heuristic. Wen et al. [18] proposed an automatic and straightforward spectral index-based approach for change detection using high-resolution imagery, replacing high-dimensional data representation with low-level features with semantic information. Ratha et al. [19] proposed a novel approach for change detection in PolSAR data by using geodesic distance on a unit sphere to quantify the distance between the Kennaugh matrices of observed and canonical scattering mechanisms. Lu et al. [3] presented a joint dictionary learning scheme that exploits the intrinsic information of different images for change detection, transforming it into a sparse representation problem where a threshold strategy is applied to identify temporal changes. Wu et al. [20] used the bag-of-visual-words model to generate a new data representation and Kernel Slow Feature Analysis (SFA) to extract nonlinear and temporally invariant features that favor identifying changes in pairs of images. Ran et al. [21] exploited one-class sparse representation classifier and kernel methods to propose unsupervised change detection for multispectral images with limited spectral bands.

Luppino et al. [22] proposed an unsupervised framework for bitemporal heterogeneous change detection using affinity matrices and image regression, where the matrices similarity is computed from co-located image patches to identify unchanged pixels and then learn a transformation to map one image to the domain of the other. Du et al. [4] proposed using two symmetric deep networks to project the input data from bi-temporal images and apply the SFA module to suppress unchanged components and highlight changed components in an unsupervised change detection scheme. Saha et al. [23] proposed a deep learning-based version for the classic change vector analysis approach, where a convolutional neural network is adopted to obtain a deep feature hyper-vector that allows the identification of changed pixels in terms of binary or types of changes.

Lin et al. [24] proposed a bilinear convolutional neural network for detecting changes in multispectral bitemporal images, which automatically learns deep feature representations and combines image information from different instants to map temporal changes. Du et al. [25] proposed a novel tri-temporal logic-verified change vector analysis approach to improve the performance of bi-temporal unsupervised change detection in remote sensing, where an additional image is incorporated for logical analysis and to validate the results obtained from bi-temporal change detection. Saha et al. [26] introduced a method for detecting changes through an unsupervised deep transcoding method using a cycle-consistent generative adversarial network to extract optical-like features from bi-temporal SAR images. Wang et al. [27] proposed an attention mechanism-based deep supervision network that extracts various features of bi-temporal images and uses them to produce a change detection map. Wu et al. [28] introduced an unsupervised model called KPCA-Mnet that utilizes kernel principal component analysis (KPCA) convolution to extract representative features from the images and map the change information into a 2-D polar domain. Shi et al. [29] introduced unsupervised multiple change detection for multispectral images using a generative representation learning network combined with a cyclic clustering technique, which refines clustering-friendly features and gradually merges similar change types into common groups.

Regarding the cited literature, only three approaches consider three [25] or more [10, 15] images for unsupervised change detection, with [10] limited to polarimetric SAR data. Although using image series beyond two instants introduces complexity to the change detection process, the availability of more information supports a better decision when separating changed from non-changed areas and allows distinguishing profiles of changes, for example, seasonal and permanent changes.

With this motivation, we propose a novel unsupervised change detection technique for image series with multiple instants. Given an image series, our approach transforms the input data into a new representation expressing the target's spectral response change over time. By using this representation, locations showing low-response variation are identified as non-change and separated from changed areas. After that, based on the introduced target's spectral representation, regions submitted to spatiotemporal modifications are discriminated between seasonal and permanent change. Statistical measures support all the distinctions mentioned above and allow the construction of a low computational cost framework. To evaluate the introduced method, experiments are carried out with synthetic data and actual remote sensing image series acquired by SAR (Sentinel-1) and multispectral (Landsat-8 OLI) sensors over distinct regions and periods.

The main contributions of this study are:

- Introduction of a fully unsupervised method;
- Proposition of a change detection approach for image time series with multiple instants;
- Categorization of change into permanent and seasonal cases;
- Formalization of a computationally light method based on statistical measures.

The article is organized as follows. Section II presents essential concepts. Section III introduces the proposed method. Section IV presents experimental results, and Section V summarizes the findings.

II. Background

The proposed technique, as detailed in Section III, utilizes data transformation, statistical tests, and classification concepts. The method's formalization has two crucial concepts: measuring the similarity between models and classifying samples. These concepts are explained in the following sections.

A. Stochastic distance for dataset comparison

Stochastic distances find their roots in divergence measures, particularly those based on Information Theory established by Shannon [30]. A divergence measure quantifies how different two statistical models are. Salicru et al. [31] introduced a generalization of divergence measures known as the h-ϕ divergence family.

Formally, let be A and B two random variables with probability density functions $f_A(\boldsymbol{x};\boldsymbol{\theta}_A)$ and $f_B(\boldsymbol{x};\boldsymbol{\theta}_B)$ over the same domain $\mathcal{X}$, the h-ϕ divergence between A and B is given by:

$$d_\phi^h(A,B) = h\left(\int_{\boldsymbol{x}\in\mathcal{X}} \phi\left(\frac{f_A(\boldsymbol{x};\boldsymbol{\theta}_A)}{f_B(\boldsymbol{x};\boldsymbol{\theta}_B)}\right) f_B(\boldsymbol{x};\boldsymbol{\theta}_B)d\boldsymbol{x}\right), \quad (1)$$

where $\phi\colon (0,\infty)\to[0,\infty)$ is a convex function, $h\colon (0,\infty)\to[0,\infty)$ is a strictly increasing function with $h(0)=0$, and $h'(t)$ is strictly positive for any $t\in(0,\infty)$.

Several widely recognized divergence measures, commonly found in the literature, can be derived from Equation (1) by selecting suitable functions h and ϕ. The symmetrization $D(A,B) = \dfrac{d_\phi^h(A,B)+d_\phi^h(B,A)}{2}$ of these measures results in h-ϕ distances, commonly referred to as "stochastic distances."

Stochastic distances between members of the same family of distributions can be transformed into a statistical goodness-of-fit test. Assuming that A and B are samples from models of the same family, a stochastic distance between them can be defined as a function of their maximum likelihood estimators $\widehat{\boldsymbol{\theta}}_A$ and $\widehat{\boldsymbol{\theta}}_B$. This leads to the notation $D(\widehat{\boldsymbol{\theta}}_A,\widehat{\boldsymbol{\theta}}_B)$ in place of $D(A,B)$. According to this, Salicru et al. [31] introduced the test statistic:

$$S_\phi^h(\widehat{\boldsymbol{\theta}}_A,\widehat{\boldsymbol{\theta}}_B) = \frac{2n_An_B}{n_A+n_B}\frac{D(\widehat{\boldsymbol{\theta}}_A,\widehat{\boldsymbol{\theta}}_B)}{h'(0)\phi''(1)}. \quad (2)$$

Under the null hypothesis $\boldsymbol{\theta}_A=\boldsymbol{\theta}_B$, and for $n_A,n_B\to\infty$ such that $n_A(n_A+n_B)\to\lambda\in(0,1)$, where n_A and n_B are the number of observations, the statistic S_ϕ^h converges to a χ^2_M distribution with M degrees of freedom, where M is the dimension of $\boldsymbol{\theta}_A$ and $\boldsymbol{\theta}_B$. The hypothesis can be rejected at level α when $\Pr\left(\chi^2_M > S_\phi^h(\widehat{\boldsymbol{\theta}}_A,\widehat{\boldsymbol{\theta}}_B)\right)\le\alpha$ [32].

B. Data classification

A classification method is a function $F\colon \mathcal{X}\to\Omega$, wherein elements from the attribute space (domain) $\mathcal{X}$ are mapped to a class in $\Omega=\{\omega_1,\omega_2,\ldots,\omega_c\}$. The myriad classification methods documented in the literature can be conceptualized as distinct strategies for modeling the function F to allocate objects in a given dataset to a thematic class in Ω; cf. Ref. [33].

Supervised learning methods necessitate information available in a reference set $\mathcal{D} = \{(\boldsymbol{x}_s,y_s)\in\mathcal{X}\times\Omega : s=1,\ldots,\#\mathcal{D}\}$ to establish the model F. The mapping between $\mathcal{X}$ and Ω as defined by F encapsulates the knowledge gleaned from the examples in $\mathcal{D}$.

III. Unsupervised mapping of temporal changes

This section introduces a novel framework for unsupervised change detection. The general pipeline, depicted in Figure 1, comprises four main steps: (i) build a temporal dynamic representation from an input image series; (ii) identify examples of targets according to distinct temporal behaviors; (iii) define a reference set to train a classification model; (iv) perform a classification of the temporal dynamic representation, obtaining a map that distinguishes unchanged areas from regions that changed according to periodic and aperiodic profiles.

This is an unsupervised learning approach, as the training is entirely conducted using samples selected by automatic processes. Sections III-A to III-D discuss and formalize the abovementioned steps.

A. Temporal dynamic representation

Let us consider a sensor producing a sequence of T images, each with $m\ge1$ channels (i.e., attributes). After a registration process, this image series, denoted as $I^{(1)},I^{(2)},\ldots,I^{(T)}$, is defined on a common support $S=\{1,2,\ldots,L\}\times\{1,2,\ldots,C\}$ with L rows and C columns. For simplicity, a position $(i,j)\in S$ is represented by an index $s=(i-1)C+j$. Optionally, by selecting a subset of attributes and/or performing local transformations, a feature image $\mathcal{I}^{(t)}$ is defined from each image $I^{(t)}$, for $t=1,\ldots,T$. This feature image is still defined on S and has $b\ge1$ attributes.

The notation $\mathcal{I}^{(t)}(s)$ refers to the feature vector $\boldsymbol{x}_s^{(t)} = [x_{s,1}^{(t)},\ldots,x_{s,b}^{(t)}]\in\mathbb{R}^b$, representing the features observed at location s and instant t. Concerning these vectors, $\mathcal{X} = \left\{\boldsymbol{x}_s^{(t)} : s\in S; t\in\{1,\ldots,T\}\right\}$ is the dataset of temporal features. Conveniently, this dataset is represented by $\mathcal{X} = \left[x_{s,1}^{(t)},\ldots,x_{s,b}^{(t)} : s\in S; t\in\{1,\ldots,T\}\right]$, forming a matrix with b columns and TLC rows.

When interested in measuring the temporal changes for a given image time series $\mathcal{I}^{(1)},\ldots,\mathcal{I}^{(T)}$, analyzing how the elements of $\mathcal{X}$ are distributed in $\mathbb{R}^b$ is a convenient starting point. The Karhunen-Loève (KL) transform [34] serves this purpose, identifying axes as a linear combination of input features that express how these features are correlated and how the data are distributed in the input space. The axes identified by the KL transform represent the relative variations as a function of time.

Formally, based on the matrix $\mathcal{X}$, we compute the covariance matrix $\boldsymbol{X}$ and its respective eigenvectors $\boldsymbol{v}_i$ and eigenvalues λ_i, for $i=1,\ldots,b$, with $\lambda_i\ge\lambda_{i+1}$. Consequently, $\boldsymbol{\lambda} = [\lambda_1,\ldots,\lambda_b]$ is the vector of eigenvalues, and $\boldsymbol{V}=[\boldsymbol{v}_1\cdots\boldsymbol{v}_b]$ is the matrix formed by eigenvectors as columns. The representation of vector $\boldsymbol{x}_s^{(t)}$ in the alternative space vector defined by the KL transform is given by $\boldsymbol{z}_s^{(t)} = \boldsymbol{x}_s^{(t)}\cdot\boldsymbol{V}\cdot\boldsymbol{\lambda}^\dagger$, where $\dagger$ is the matrix transposition operation.

About this alternative representation, the change observed at s between instants t and $t+1$ can be expressed as $\left(\boldsymbol{x}_s^{(t+1)}-\boldsymbol{x}_s^{(t)}\right)\cdot\boldsymbol{V}\cdot\boldsymbol{\lambda}^\dagger$. Moreover, the cumulative changes between t and $t+k$ are obtained by:

$$\left(\boldsymbol{x}_s^{(t+1)}-\boldsymbol{x}_s^{(t)}\right)\cdot\boldsymbol{V}\cdot\boldsymbol{\lambda}^\dagger + \left(\boldsymbol{x}_s^{(t+2)}-\boldsymbol{x}_s^{(t+1)}\right)\cdot\boldsymbol{V}\cdot\boldsymbol{\lambda}^\dagger + \cdots + \left(\boldsymbol{x}_s^{(t+k)}-\boldsymbol{x}_s^{(t+k-1)}\right)\cdot\boldsymbol{V}\cdot\boldsymbol{\lambda}^\dagger,$$

representing the sum of consecutive changes over the observed period.

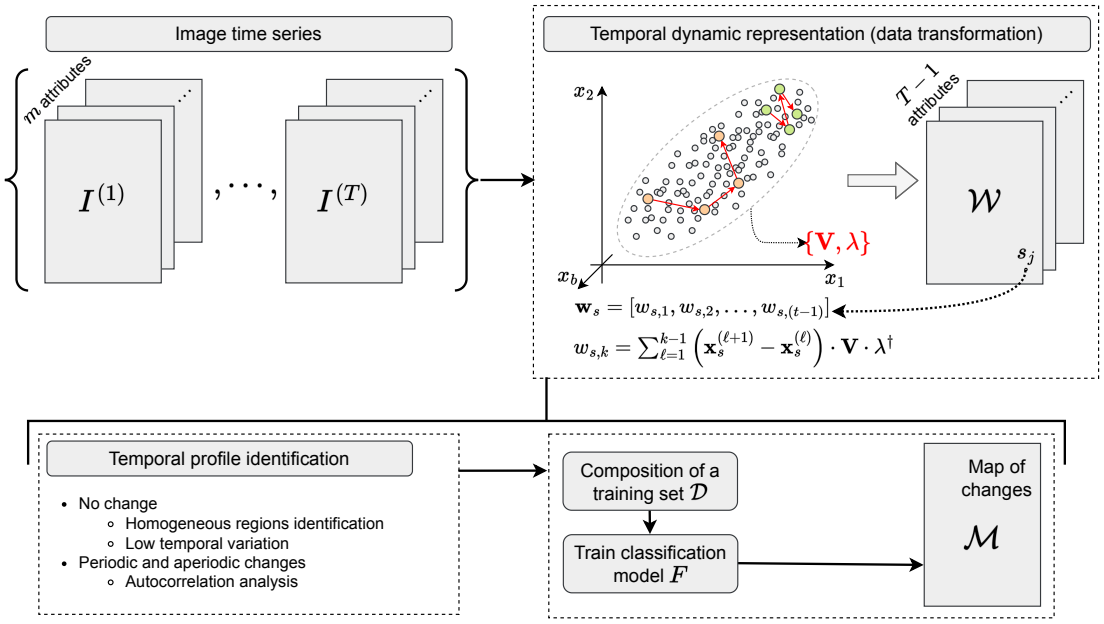

Fig. 1. Framework of the proposed approach for change detection in extensive image series.

Recalling our interest in analyzing the dynamic changes at each position $s \in S$ over time, we define the vector $\boldsymbol{w}_s = [w_{s,1}, w_{s,2}, \ldots, w_{s,T-1}] \in \mathbb{R}^{(T-1)}$ that encodes the temporal displacements, whose components are determined by:

$$w_{s,k} = \sum_{\ell=1}^{k-1} \left(\boldsymbol{x}_s^{(\ell+1)} - \boldsymbol{x}_s^{(\ell)}\right)^{\dagger} \cdot \boldsymbol{V} \cdot \boldsymbol{\lambda}^{\dagger}. \tag{3}$$

Applying Equation (3) to every $s \in S$ of the input feature image series $\mathcal{I}^{(1)}, \ldots, \mathcal{I}^{(T)}$ (i.e., a dataset with $L \times C \times b \times T$ dimensions) reduces it to an image with $(T-1)$ features and same support S (i.e., a dataset with $L \times C \times (T-1)$ dimensions), denoted herein as $\mathcal{W}$.

Additionally, it should be noted that $\boldsymbol{w}_s$ is formulated to display the temporal evolution at s with respect to the input features in relation to the structure of $\mathcal{X}$. Locations subjected to significant changes over time are expected to produce feature vectors $\boldsymbol{x}_s^{(t)}$ that migrate to a position of the input data-space different from the position occupied in the initial instants of the time series. Similarly, periodically-behaved components in $\boldsymbol{w}_s$ may indicate locations subjected to temporally-recurrent changes. In the same sense, $\boldsymbol{w}_s$ with similar components represent non-change case. The following sections discuss procedures based on the temporal displacement vector to identify the mentioned situations.

B. Non-change case

Identifying regions within the support S that exhibit both low spatial and spectral variability is crucial for pinpointing instances of targets that remain unchanged over time. A straightforward approach to quantify spectral-temporal variation involves computing the image $\mathcal{V}$, expressing the sample standard deviation of $\boldsymbol{w}_s$ at each $s \in S$, where:

$$\mathcal{V}(s) = \hat{\gamma}(\boldsymbol{w}_s) = \sqrt{\frac{1}{T-1} \sum_{\ell=1}^{T-1} (w_{s,\ell} - \overline{w}_s)^2}, \tag{4}$$

where

$$\overline{w}_s = \frac{1}{T-1} \sum_{\ell=1}^{T-1} w_{s,\ell}. \tag{5}$$

To address spatial variability, Negri et al. [35] proposed an approach to identify homogeneous regions, indicating low spatial variability in an input image. This method can be applied to $\mathcal{V}$ to identify regions resistant to change over time. Positions s_i are chosen as centers of blocks (square regions) $\mathcal{B}(s_i, \rho) = \{q \in S : \max\{|s_i - q|\} < \rho\}$ with side $2\rho + 1$. Positions s_i are selected with $\rho = \frac{\min\{L, C\} - 1}{2}, \ldots, 2, 1$, ensuring no overlap with other homogeneous regions. Figure 2(a) illustrates the relationship between the support and block sizes.

Regarding a block $\mathcal{B}(s_i, \rho)$, regular-shaped subsets $\mathcal{B}_\ell(s_i, \rho)$, for $\ell = 1, \ldots, 6$, comprising part of the entire block, are defined. Denoting s_i by the planar coordinate form (r_i, c_i), we have the following subsets:

$$\begin{aligned}
\mathcal{B}_1(s_i, \rho) &= \{(p, q) \in \mathcal{B}(s_i, \rho) : c_i - \rho < q < c_i\}, \\
\mathcal{B}_2(s_i, \rho) &= \{(p, q) \in \mathcal{B}(s_i, \rho) : c_i < q < c_i + \rho\}, \\
\mathcal{B}_3(s_i, \rho) &= \{(p, q) \in \mathcal{B}(s_i, \rho) : q \geq p\}, \\
\mathcal{B}_4(s_i, \rho) &= \{(p, q) \in \mathcal{B}(s_i, \rho) : r_i - \rho < p < r_i\}, \\
\mathcal{B}_5(s_i, \rho) &= \{(p, q) \in \mathcal{B}(s_i, \rho) : r_i < p < r_i + \rho\}, \text{ and} \\
\mathcal{B}_6(s_i, \rho) &= \{(p, q) \in \mathcal{B}(s_i, \rho) : q \leq p\},
\end{aligned}$$

illustrated in Figure 2(b).

Given these definitions and the scalar representation by $\mathcal{V}$ for spectral-temporal variations on S, a block $\mathcal{B}(s_i, \rho)$ is considered

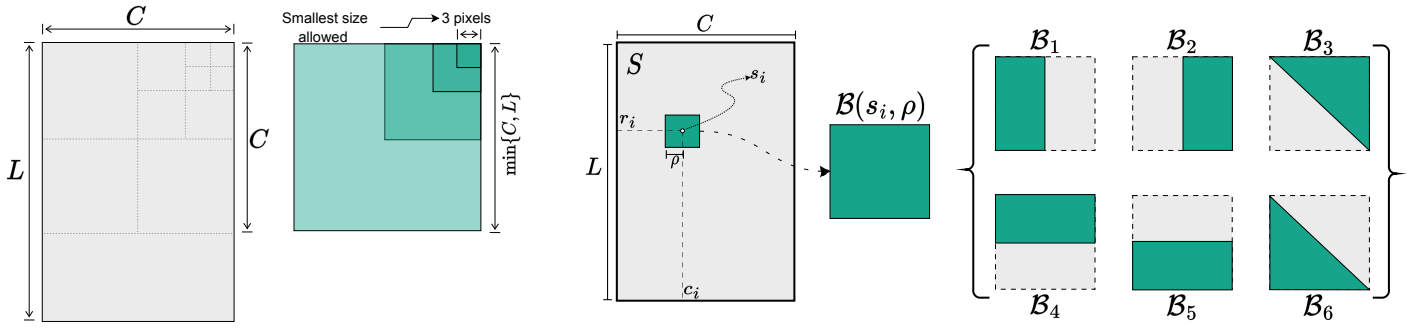

(a) The relation between support and blocks size.

(b) A block and its parts.

Fig. 2. Block-shaped structures taken to assess the block homogeneity.

homogeneous if the distribution of values $\hat{\gamma}(\boldsymbol{w}_s) \in \mathbb{R}$ observed inside it is similar to the distributions of the values observed in each subset $\mathcal{B}_\ell$, for $\ell = 1, \ldots, 6$. The following rule expresses this verification:

$$\max_{\ell=1,\ldots,6} \Pr\left(\chi^2_M > S^\phi_h(\hat{\boldsymbol{\theta}}, \hat{\boldsymbol{\theta}}_\ell)\right) < \alpha_H. \tag{6}$$

where α_H is a threshold based on the statistical properties of S^ϕ_h under the null hypothesis of no-change.

In Equation (6), $S^\phi_h(\cdot,\cdot)$, as defined in Section II-A, depends on the considered family of distributions and the chosen stochastic distance, determined by the functions h and ϕ. A convenient choice is the Bhattacharya distance defined by $h(y) = -\log(1-y)$ and $\phi(x) = -\sqrt{x} + (x+1)/2$. Assuming that the values $\hat{\gamma}(\boldsymbol{w}_s)$ in $\mathcal{B}$ and $\mathcal{B}_\ell$ are modeled by Gaussian distributions with parameters $\boldsymbol{\theta} = (\mu, \sigma)$ and $\boldsymbol{\theta}_\ell = (\mu_\ell, \sigma_\ell)$, the Bhattacharya distance is expressed as:

$$D(\widehat{\boldsymbol{\theta}}, \widehat{\boldsymbol{\theta}}_\ell) = \frac{1}{4}\frac{\mu - \mu_\ell}{\sigma^2 + \sigma^2_\ell} + \frac{1}{2}\ln\frac{\sigma^2 + \sigma^2_\ell}{2\sigma\sigma_\ell}. \tag{7}$$

The processes discussed above allows to identify a set $\mathcal{H}$ of positions s inserted into homogeneous blocks that ensure low spatial variability with a significance/confidence level α_H. Next, limited to these locations $s \in \mathcal{H}$, it becomes necessary to segregate the high spectral occurrences. To achieve this, a threshold η is applied to $\hat{\gamma}(\boldsymbol{w}_s)$ values. The empirical rule presented by Negri and Frery [36] is an alternative to classic algorithms [37, 38] effective when the data follow a positive and heavy-tailed distribution, as usually observed in deviation measures such as those expressed by $\mathcal{V}$. This rule is defined by:

$$\eta = \arg \max_{\widetilde{z} \in [\gamma_{\min}, \gamma_{\max}]} \frac{C_1 C_2 (C_1 + C_2)}{A_1 A_2 (A_1 + A_2)}, \tag{8}$$

where:

$$\begin{aligned}
C_1 &= \int_{\gamma_{\min}}^{\widetilde{z}} g(z)dz, \\
C_2 &= \int_{\widetilde{z}}^{\gamma_{\max}} g(z)dz, \\
A_1 &= (\widetilde{z} - \gamma_{\min}) \max_{z \in [\gamma_{\min}, \widetilde{z}]} \{g(z)\}, \text{ and} \\
A_2 &= (\gamma_{\max} - \widetilde{z}) \max_{z \in [\widetilde{z}, \gamma_{\max}]} \{g(z)\},
\end{aligned}$$

where $g(\cdot)$ represents the probability density function of $\hat{\gamma}(\boldsymbol{w}_s)$ for $s \in \mathcal{H}$, with values limited to $[\gamma_{\min}, \gamma_{\max}]$.

While C_1 and C_2 represent the areas under g below and above η, respectively, A_1 and A_2 denote the areas of the rectangles enclosing g within $[\gamma_{\min}, \eta]$ and $[\eta, \gamma_{\max}]$, respectively. The objective is to achieve the optimal equilibrium for both ratios $\frac{C_1}{A_1}$ and $\frac{C_2}{A_2}$. An imbalanced selection for η leads to either $\frac{C_1}{A_1} \to 0$ or $\frac{C_2}{A_2} \to 0$, resulting in $\frac{C_1 C_2 (C_1 + C_1)}{A_1 A_2 (A_1 + A_2)} \to 0$. Figure 3 illustrates these components, where C_1 and C_2 denote the dotted and dashed areas under g; A_1 and A_2 represent the red and green rectangles over g. The optimal balance is achieved when the areas under the curve are closest to the rectangle area.

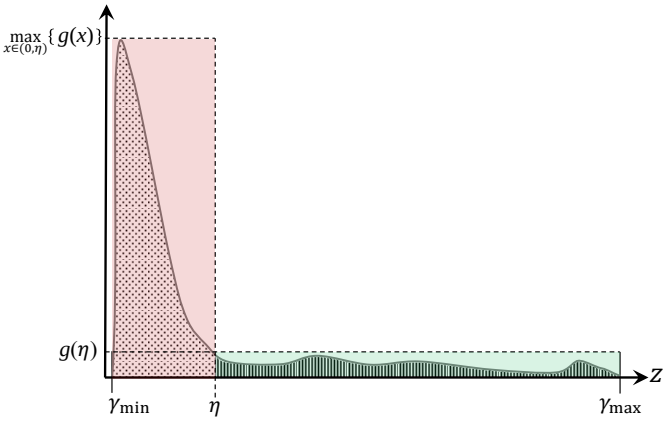

Fig. 3. Empirical rule to determine the threshold η.

The processes covered by Equations (4) to (8) allow us to identify locations in S that suggest the absence of temporal changes. This information is conveniently adopted to compose a reference set required to model classification functions, as discussed in Section III-D.

C. Change case

To distinguish changes based on different profiles, particularly periodic (seasonal) and aperiodic (permanent) changes, additional statistics are derived from $\mathcal{W}$. Limited to locations s such that $\mathcal{V}(s) > \eta$, is computed the partial autocorrelation

vector $\boldsymbol{a}_s = [a_{s,1}, a_{s,2}, \ldots, a_{s,T-2}]$, which components are given by:

$$a_{s,\ell} = \frac{\sum_{k=1}^{(T-1)-\ell-1}(w_{s,k} - \overline{w}_s)(w_{s,(k+\ell)} - \overline{w}_s)}{\sum_{k=1}^{(T-1)-1}(w_{s,k} - \overline{w}_s)^2}, \quad (9)$$

where

$$\overline{w}_s = \frac{1}{T-2}\sum_{k=1}^{T-2} w_{s,k}. \quad (10)$$

The vectors obtained from Equation (9) are conveniently depicted by the image $\mathcal{A}$, where $\boldsymbol{a}_s = \mathcal{A}(s)$. A permanent temporal change is identified when a linear relation is observed among the components of $\boldsymbol{a}_s$. We apply the F-test [39] to assess whether a linear model $\phi(a) = \beta_0 + a \cdot \beta_1$ adequately fits the components of $\boldsymbol{a}_s$. Assuming a random variable Z that follows the distribution $F_{q-1,T-2-q}$, with $q = 2$ representing the number of parameters in $\phi(\cdot)$, a linear relation (i.e., $\beta_1 \neq 0$, indicating rejection of the null hypothesis $H_0 : a_{s,\ell} = \beta_0$; for $\ell = 1, \ldots, T-2$) is observed when the probability $p_s = 1 - \Pr(Z > f_s)$ is less than the adopted significance level α_F. The statistic f_s is computed as:

$$f_s = \big((T-2)-2\big)\left(\frac{\sum_{\ell=1}^{T-2}(a_{s,\ell} - \phi(a_{s,\ell}))^2}{\sum_{\ell=1}^{T-2}(a_{s,\ell} - \overline{a}_s)^2} - 1\right), \quad (11)$$

where

$$\overline{a}_s = \frac{1}{T-2}\sum_{\ell=1}^{T-2} a_{s,\ell}. \quad (12)$$

D. Induced reference set and classifier modeling

The formalization presented in Sections III-B and III-C provides procedures and rules to identify locations s representing a potential case of no-change, periodic, or aperiodic change. However, it should be noted that the union of all these identified locations may not entirely cover the support S. To account for this, a classifier modeled by a reference set constituted by the identified cases is a suitable way to extrapolate and deliver a map of the spatiotemporal dynamics.

Formally, let us assume the set of classes $\Omega = \{\omega_1, \omega_2, \omega_3\}$ and $\overline{S}$ as a set of identified locations that represents cases of non-change, periodic, or aperiodic change. We define the reference set $\mathcal{D} = \big\{(\boldsymbol{w}_s, y_s) \in \mathbb{R}^{T-1} \times \Omega \colon s \in \overline{S}\big\}$ such that:

- $y_s = \omega_1$ if $s \in \mathcal{H}$ and $\mathcal{V}(s) < \eta$ — indicating a non-change case;
- $y_s = \omega_2$ if $\mathcal{V}(s) \geq \eta$ and $p_s \geq \alpha_F$ — indicating a periodic change case;
- $y_s = \omega_3$ if $\mathcal{V}(s) \geq \eta$ and $p_s < \alpha_F$ — indicating an aperiodic change case.

Figure 4 summarizes how the elements formalized in Sections III-A to III-C interact with the input data to identify examples of non-change, periodic and aperiodic changes. Finally, the set $\mathcal{D}$ that contains the identified examples is employed to model a classifier $F \colon \mathbb{R}^{T-1} \to \Omega$ and then apply it to each position s in $\mathcal{W}$, providing as outcome a map $\mathcal{M}$ that spatially distinguishes locations according to the classes of Ω.

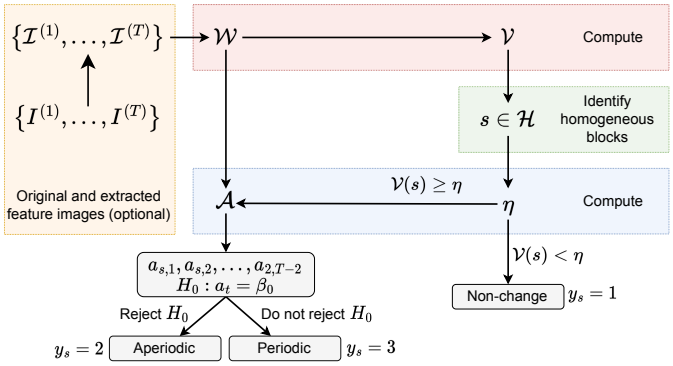

Fig. 4. Mathematical components in the proposed approach and their interactions..

IV. Experiments

In Sections IV-A and IV-B we present the use of the proposed technique on simulated and actual remote sensing datasets, respectively. The simulated dataset is generated using multivariate Gaussian distributions, and its parameters are determined from targets selected in remote sensing image series. The experiments with actual remote sensing data involve two distinct case studies.

We compare our method to the WECS method [15], which, according to the bibliographic discussion presented in Section I, allows mapping regions of change and non-change through image series of multiple instants. For the sake of a fair comparison with the alternative method, the multiclass results provided by the proposed approach are binarized by merging the "periodic and aperiodic cases" as a single "change case", before computing accuracy measures. We use the kappa coefficient of agreement [40] and the F1-Score [41] to report the accuracy on multiclass and binary cases, respectively.

The Maximum Likelihood Classifier (MLC) [42] with multivariate Gaussian distribution to model class likelihood, and the Support Vector Machine (SVM) [43] are tested as classification model F. Furthermore, in the following discussions, we refer to the proposed method as UTCM, once it performs an *unsupervised temporal change mapping*. Consequently, UTCM+MLC and UTCM+SVM indicate that the proposal is equipped with the MLC and SVM methods as classifiers, respectively.

The experiments were carried out on a computer with an Intel Core i7 processor and 32 GB of RAM running the Debian Linux version 11 operating system. The platform used was IDL (Interactive Data Language) version 8.9.

A. Experiment with simulated data

Details about the process to simulate image series are presented in Section IV-A1. Subsequently, the proposed and the alternative approaches are applied in the simulated series and the results are compared.

1) Simulation process: We simulate an image series with simulated targets with distinct temporal profiles. The profiles include:

- No trend, representing a case of non-change;

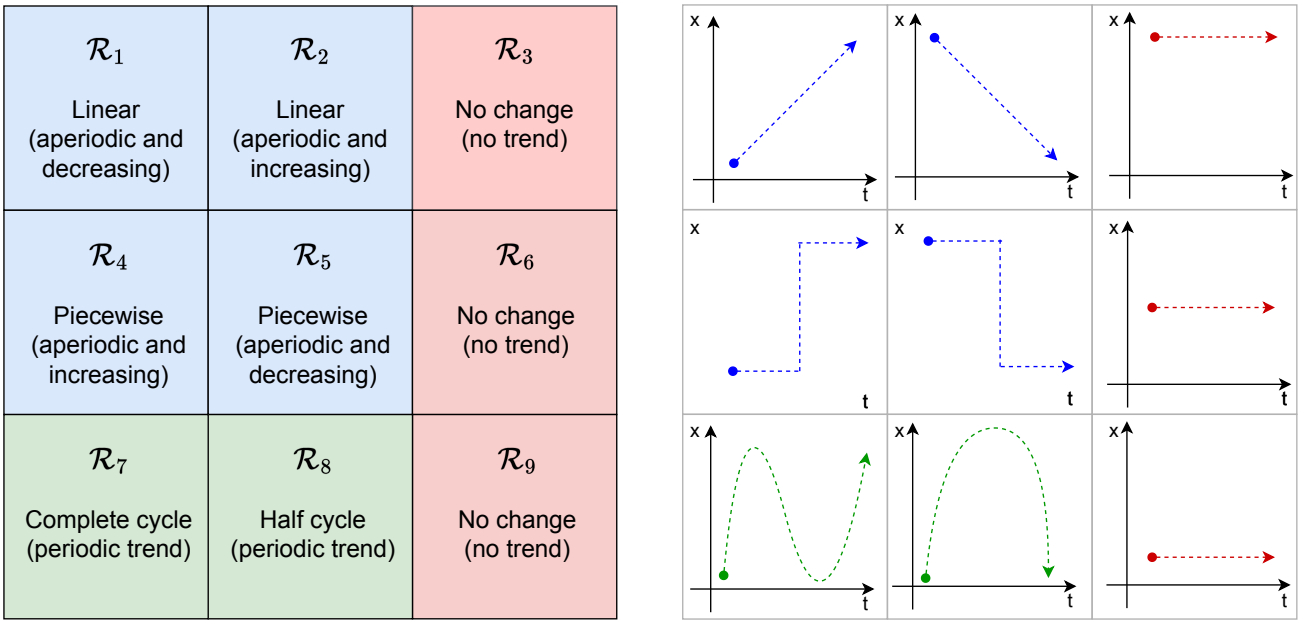

(a) Phantom and regions.

(b) Temporal profiles assigned to each region.

Fig. 5. The phantom image with nine regions, and their respective change profiles.

- Increasing and decreasing linear tendencies, representing aperiodic change cases;
- Piecewise tendencies, representing aperiodic profiles expressing a change from a constant regime to another;
- Periodic tendencies, drawn as a complete or a half cycle.

Figure 5(a) shows the *phantom image* adopted to simulate the image series. This cartoon model is made up of nine regions, $\mathcal{R}_1$ to $\mathcal{R}_9$, each with 100×100 pixels. Additionally, a specific temporal profile is assigned to each region, as elucidated in Figure 5(b).

The temporal profiles are simulated based on samples observed from actual remote sensing image series, which determine the parameters of multivariate Gaussian distributions.

Suppose an image series $\mathcal{I}^{(1)}, \ldots, \mathcal{I}^{(T)}$, defined in the feature space $\mathcal{X}$, and a sample $\mathcal{E} = \{\boldsymbol{x}_s^{(\ell)} : \ell = 1, \ldots, T;\ s \in E \subset S\}$, which gathers feature vectors from the image series regarding a region E of the support S. Based on the information in $\mathcal{E}$, mean and standard deviation vectors $\boldsymbol{\mu}_\ell$ and $\boldsymbol{\sigma}_\ell$, for $\ell = 1, \ldots, T$, are calculated. These vectors summarize the tendency and deviation over the series. An image series is simulated according to the profiles depicted in Figure 5 through Equations (13) to (17). Specifically, Equation (13) defines a model to simulate feature vectors according to an aperiodic and linear trend, which are assigned to regions $\mathcal{R}_1$ and $\mathcal{R}_2$. Similarly, Equation (14) draws the vectors for regions $\mathcal{R}_4$ and $\mathcal{R}_5$ according to an aperiodic and piecewise trend. The feature vectors for regions $\mathcal{R}_7$ and $\mathcal{R}_8$ are obtained using Equations (15) and (16). Lastly, Equation (17) is responsible for simulating the behavior of the regions $\mathcal{R}_3$, $\mathcal{R}_6$ and $\mathcal{R}_9$, which represent targets that do not change over time.

$$\boldsymbol{x}_s^{(t)} \sim N\left(\widetilde{\boldsymbol{\mu}}^{(t)}, \overline{\Sigma}^{(t)}\right),\ t = 1, \ldots, T; \tag{13}$$

$$\boldsymbol{x}_s^{(t)} \sim \begin{cases} N\left(\boldsymbol{\mu}_1 \psi_t, \overline{\Sigma}^{(t)}\right), & 1 \leq t < \frac{T}{2} \\ N\left(\boldsymbol{\mu}_T \psi_t, \overline{\Sigma}^{(t)}\right), & \frac{T}{2} \leq t \leq T \end{cases}; \tag{14}$$

$$\boldsymbol{x}_s^{(t)} \sim N\left(\frac{\overline{\boldsymbol{\mu}}}{2}\psi_t\left(\sin\left(\frac{\pi t}{T}\right) + \overline{\boldsymbol{\mu}}\right), \overline{\Sigma}^{(t)}\right),\ t = 1, \ldots, T; \tag{15}$$

$$\boldsymbol{x}_s^{(t)} \sim N\left(\frac{\overline{\boldsymbol{\mu}}}{2}\psi_t\left(\sin\left(\frac{2\pi t}{T}\right) + \overline{\boldsymbol{\mu}}\right), \overline{\Sigma}^{(t)}\right),\ t = 1, \ldots, T; \tag{16}$$

and

$$\boldsymbol{x}_s^{(t)} \sim N\left(\overline{\boldsymbol{\mu}}\psi_t, \overline{\Sigma}^{(t)}\right),\ t = 1, \ldots, T; \tag{17}$$

where $\widetilde{\boldsymbol{\mu}}^{(t)} = t \cdot \frac{\boldsymbol{\mu}_T - \boldsymbol{\mu}_1}{T} \cdot \psi_t$; $\overline{\boldsymbol{\mu}} = \frac{\sum_{\ell=1}^{T} \boldsymbol{\mu}_\ell}{T}$; and $\overline{\Sigma}^{(t)} = \text{diag}\left(\psi_t \cdot \frac{\boldsymbol{\sigma}_1 + \boldsymbol{\sigma}_T}{2}\right) \cdot \mathbf{I} \cdot \text{diag}\left(\psi_t \cdot \frac{\boldsymbol{\sigma}_1 + \boldsymbol{\sigma}_T}{2}\right)$, with $\mathbf{I}$ representing the identity matrix and $\psi_t \sim U(0.95, 1.05)$ is responsible for introducing changes in the parameters.

To simulate a 50-instant image series, were selected nine samples from the dual-polarization (VV and VH) SAR image series adopted in the experiments of Section IV-B. Figure 6 depicts the selected samples and the respective mean amplitude backscatter representing piecewise linear trend cases, complete and half cycles, and non-change profiles.

Figure 7 shows the first and last instants (i.e., $t = 1$ and $t = 50$) of the simulated image series. According to these outputs, one may observe that the regions that do not represent changes ($\mathcal{R}_1$, $\mathcal{R}_6$, and $\mathcal{R}_9$) are similar at both instants. The region $\mathcal{R}_8$ represents a periodic change with equal initial and final instants (due to its profile). Furthermore, the other regions

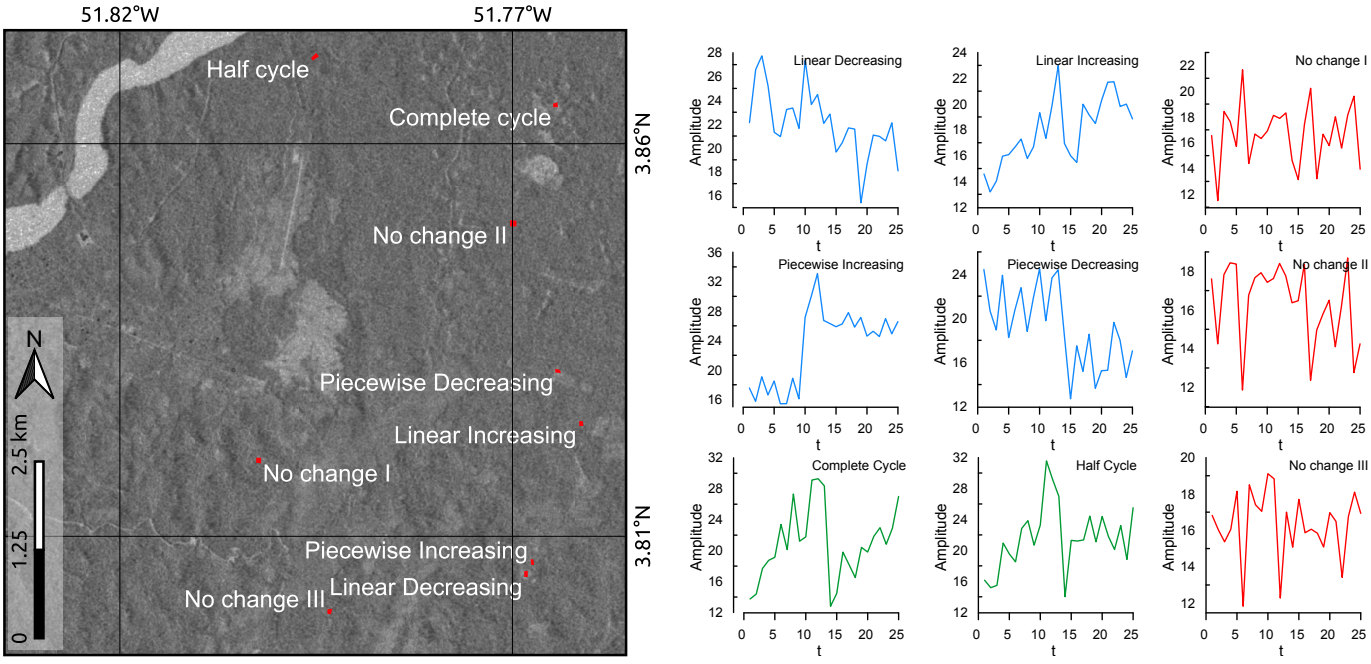

(a) Selected samples. Representation using the amplitude from the initial image of the SAR series.

(b) Temporal profile of each selected sample.

Fig. 6. Samples selected from the SAR image series, defined in Section IV-B, and their respective temporal profiles.

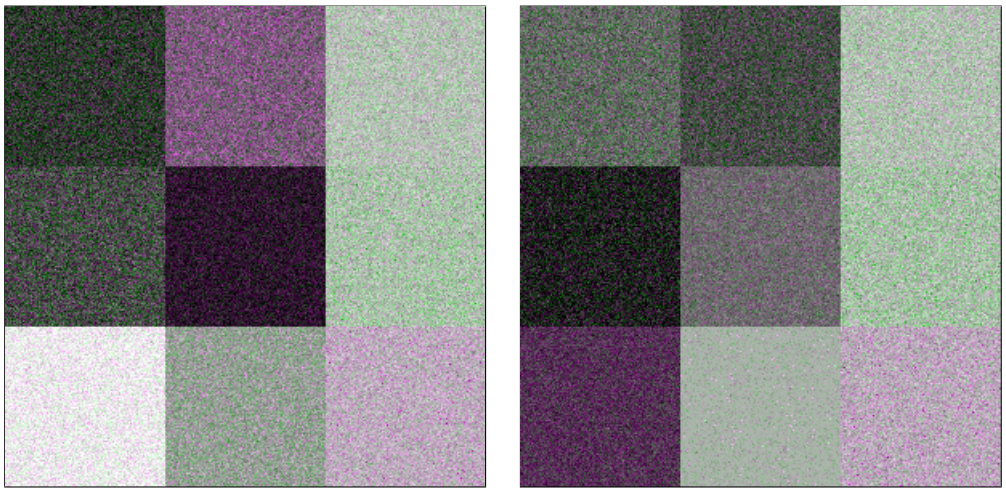

(a) $\mathcal{I}^{(1)}$

(b) $\mathcal{I}^{(50)}$

Fig. 7. The first and last instants of the simulated image series in R(VV)G(VH)B(VV) color composition.

(i.e., $\mathcal{R}_1$, $\mathcal{R}_2$, $\mathcal{R}_4$, and $\mathcal{R}_5$) present an inversion of behavior when comparing the first and last instants.

2) Results with simulated data: The image series simulated in the previous section was submitted to the alternative (WECS) proposed (UTCM) methods outlined in Section III. Various parameter configurations were thoroughly tested, considering values of α_B and α_F from the sets $\{0.1, 0.15, 0.2, \ldots, 0.95\}$ and $\{0.01, 0.05, 0.1\}$, respectively. As mentioned above, the classification models used were the Maximum Likelihood Classifier (MLC) [42] and Support Vector Machine (SVM) [43]. The SVM utilized the radial basis kernel function, and the parameters (penalty C and kernel basis scale γ) were adjusted through a grid-search procedure with $C \in \{1, 10, 10^2, 10^3\}$ and $\gamma \in \{0.001, 0.005, 0.01, 0.05, 0.1\}$. This parameter tuning process adopts the overall accuracy as objective function, which is computed by a 5-fold cross-validation on the reference set ($\mathcal{D}$ – Section III-D). Concerning the alternative method, distinct wavelet families (Haar, Daubechis of orders 2 and 4; Symlets of orders 2 and 4; and Coiflets of order 4) and resolutions (2, 4, 6, 8, and 10). For more details, please refer to Fonseca et al. [15].

Figure 8 summarizes the accuracy results of the proposed method using MLC and SVM as classifiers for each combination of α_B and α_F. The accuracy values, represented

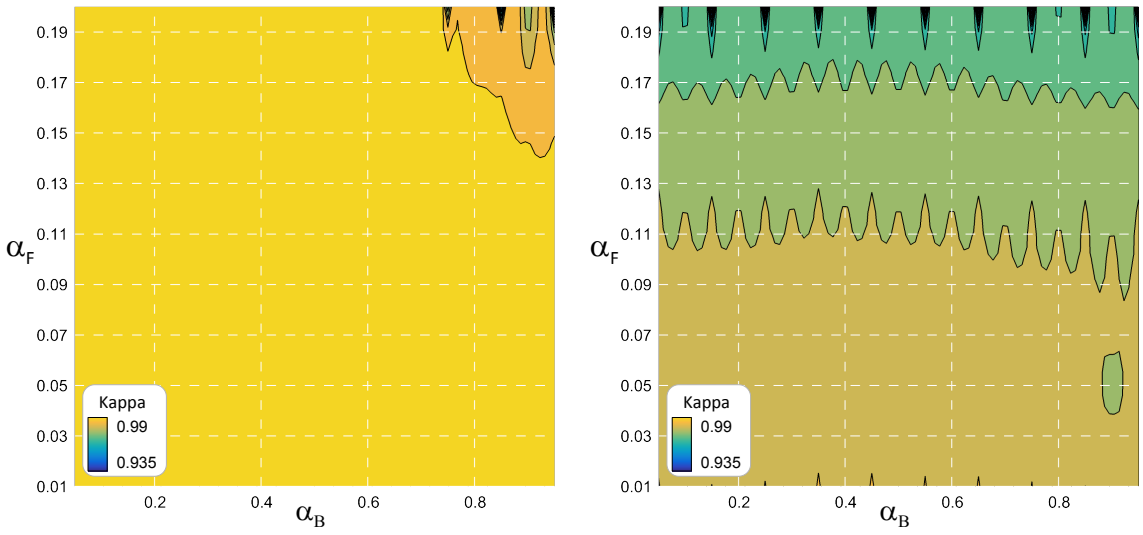

(a) UTCM+MLC (b) UTCM+SVM

Fig. 8. Performance on the simulated image series, in terms of the kappa coefficient, for distinct classification models and parameters α_B and α_F.

TABLE I
PERFORMANCE SUMMARY OF THE ANALYZED METHODS REGARDING THE MULTICLASS AND BINARY CHANGE DETECTION. VALUES IN PARENTHESIS ARE THE VARIANCE OF KAPPA.

Multiclass (kappa)		**Binary (F1-Score)**		
UTCM+MLC	UTCM+SVM	WECS	UTCM+MLC	UTCM+SVM
0.995 (0.896×10^{-7})	0.990 (0.170×10^{-6})	0.995	0.997	0.998

by the kappa coefficient, are computed with reference to the classes defined in the phantom image (i.e., no change, periodic, and aperiodic changes). In this first experiment battery, when equipped with the MLC classifier, the proposed method is less sensitive to α_B and α_F parameters compared to using the SVM method. The highest kappa values achieved by UTCM+MLC occur under $\alpha_B = 0.35$ and $\alpha_F = 0.09$. Similarly, for UTCM+SVM, the best performance is assigned to $\alpha_B = 0.35$ and $\alpha_F = 0.08$.

Figure 9 presents the best results achieved by the alternative and proposed methods. The respective accuracy values are reported in Table I. When using the MLC model, the kappa coefficient and the variance of kappa are equal to 0.994 and 0.896×10^{-7}, respectively. For the SVM model, these measures are equal to 0.99 and 0.169×10^{-6}. Applying a hypothesis test to compare the kappa values [40], the resulting p-value $\ll 10^{-5}$ indicates the superiority, with a significance of $1\,\%$, of using the MLC model in the proposed approach.

Reinterpreting the UTCM+MLC and UTCM+SVM results as a binary outcome (i.e., periodic and aperiodic classes merged into a single "change" class), and computing the F1-Score, one may verify a slight difference of the introduced approach compared to the WECS method (best result with Haar wavelet family and resolution of 1), as shown in Table I. This divergence occurs mainly due to the WECS errors in the extreme right edge.

In conclusion, the results of this initial experiment demonstrate the capability of the proposed approach to identify different temporal profiles expressed in the simulated image series. Additionally, a slightly superior accuracy is achieved when the MLC method is adopted as the classifier. Discussions regarding the computational run-time are presented in the next section.

B. Experiments with remotely sensed data

In addition to experiments with simulated data, the proposed approach is applied in two study cases with remotely sensed images. Figure 10 shows the location of the areas where each study case takes place. The first study case considers a 25-instant image series acquired between December 26th, 2015, and December 3rd, 2017, by the SAR sensor onboard the Sentinel-1 satellite, over a forest region (Area 1) on the border of Brazil and French Guiana. Each image contains the amplitude signal backscatters relative to the VV and VH polarizations, with a spatial resolution of $10\,\mathrm{m}$ and a support of 893×888 pixels. Regarding the second study case, a 22-instant image series acquired by the Landsat-8 OLI sensor between December 9th, 2013, and July 15th, 2021, with $30\,\mathrm{m}$ spatial resolution, support of 1167×1071 pixels, and bands from green to NIR wavelengths. The region covered in this case (Area 2) encompasses a region of the city of São Félix do Xingu, Brazil.

Figure 11 shows the spatial distribution of periodic, aperiodic, and non-change samples for each study area. Table II summarizes the size of the reference samples obtained by visual inspection, which were taken to measure the accuracy of the proposed method.

It is worth mentioning that the OLI images were obtained in "level-2 processing," including a built-in atmospheric correction. The image series was pre-processed by masking any occurrence of clouds and shadows, with missing values being interpolated from the previous immediate data or posterior in the case of

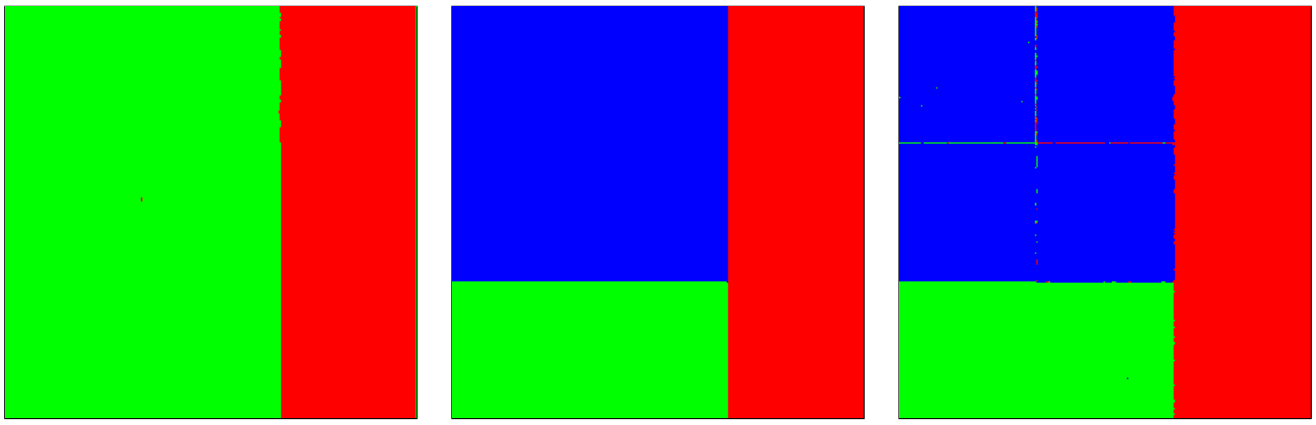

(a) WECS (Binary) (b) UTCM+MLC (c) UTCM+SVM

Fig. 9. Best result achieved on the simulated dataset by the proposed and alternative methods. Binary case: Non-change Change Multiclass case: Non-change Periodic Aperiodic

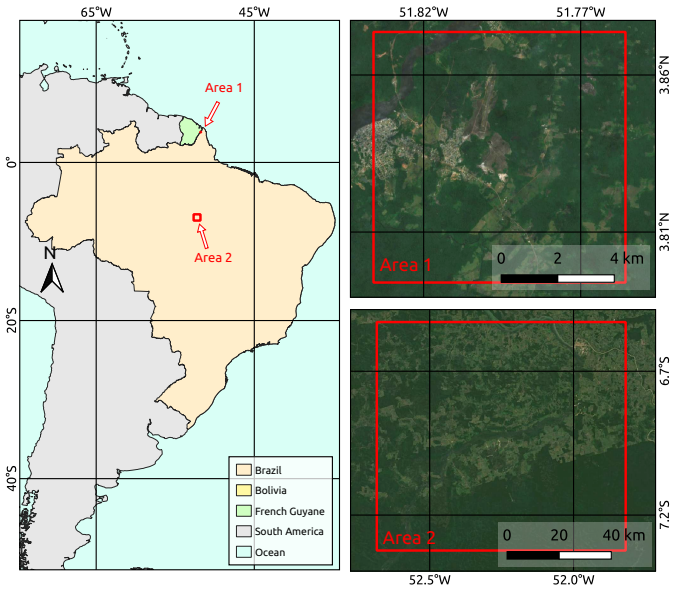

Fig. 10. Study area locations.

the first instant. A 3×3 average low-pass filtering was applied to the SAR images as a simple approach to reduce speckle.

TABLE II
SUMMARY OF NON-CHANGE, PERIODIC AND APERIODIC REFERENCE SAMPLES.

	Non-change	**Aperiodic**	**Periodic**
Area 1	2020	2079	2203
Area 2	1227	1299	1353

Following an experiment design similar to those described at the beginning of Section IV-A2, a sensitivity analysis of the proposed method is performed with respect to the parameters α_B and α_F. Figures 12 and 13 show the results for Areas 1 and 2, respectively. In both cases, and independent of the adopted classification model, better performances are related to small values of α_B. Regarding the parameter α_F, convenient choices comprise values above 0.11 for Area 1. In Area 2, this parameter does not have a strong influence on performance.

According to the discussion above, the parameter pair (α_B, α_F) assigned to the best performance in Area 1, when adopting the MLC and SVM classifiers, is equal to $(0.35, 0.17)$ and $(0.2, 0.15)$, respectively. The temporal dynamic maps related to these configurations are shown in Figure 14. Regarding using the MLC method, the computed kappa coefficient and kappa variance are 0.735 and 0.493×10^{-4}. In the same sense, when using the SVM method, the calculated kappa coefficient and variance are 0.655 and 0.559×10^{-4}. Based on the values reported, the result obtained using the MLC method is superior to those using the SVM method with a significance of $1\,\%$. Comparing these results from a qualitative point of view, although the salt-and-paper effect is present in both results, the regions of aperiodic change profile are better distinguished by the MLC method.

Concerning the results for Area 2, when using the MLC method, the calculated kappa coefficient and variance are 0.760 and 0.781×10^{-4}, respectively. When using the SVM method, it is computed a kappa and variance of 0.710 and 0.904×10^{-4}. A statistical test to compare the reported kappa values shows a p-value of 4.6×10^{-5}, allowing us to conclude that the MLC is superior to the SVM method with $1\,\%$ significance.

Regarding the WECS approach, the utmost accurate result was achieved using the Daubechies wavelet family of order 2 and a resolution of 3 for Area 1. On the other hand, for Area 2, the Coiflet of order 4 and resolution of 5 provided the most precise outcome. According to these parameters, the calculated F1-Scores for Areas 1 and 2 are 0.818 and 0.812, respectively. By reinterpreting the UTCM+MLC results as binary change maps, the computed F1-Scores are 0.977 and 0.964 on Areas 1 and 2. Regarding UTCM+SVM, the calculated scores for Areas 1 and 2 are 0.966 and 0.963, respectively. These accuracy values, reported in Table III, corroborate the output maps depicted in Figures 14 and 15, where a better delimitation is perceptive between areas of change and non-change when the proposed technique is employed. Furthermore, from a qualitative point of view, a slight noise intensity is observed

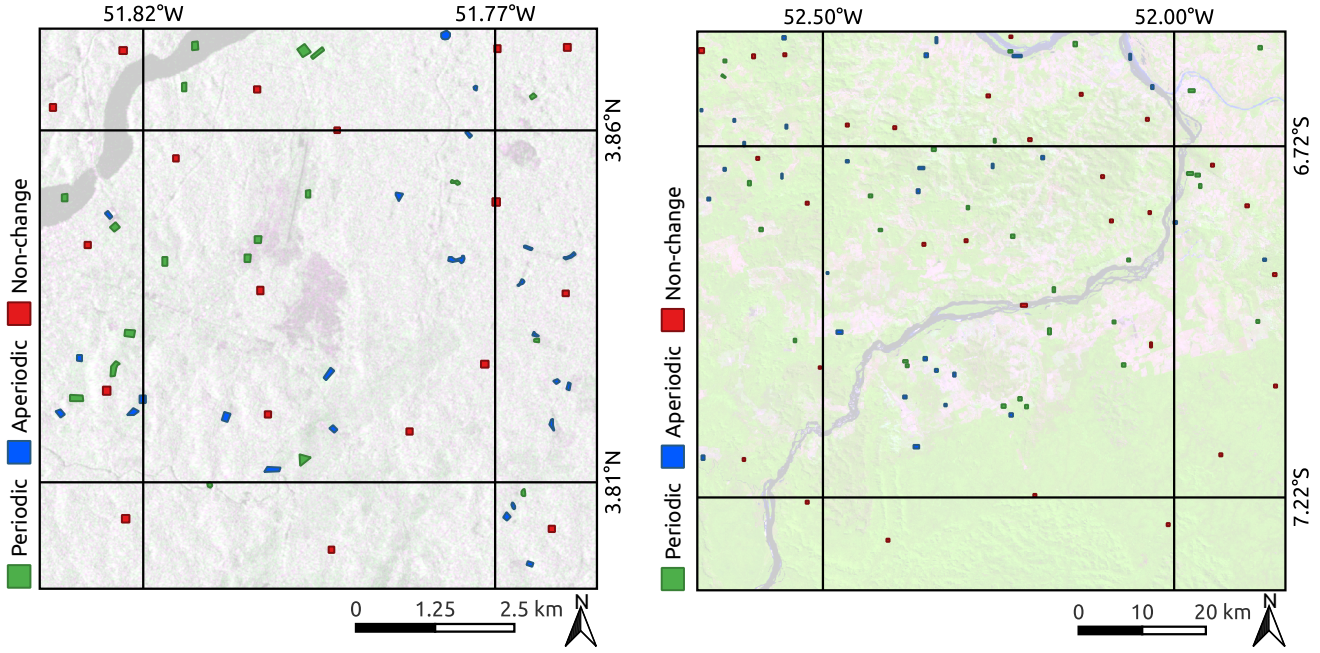

(a) Area 1

(b) Area 2

Fig. 11. Reference samples for Areas 1 and 2.

TABLE III
PERFORMANCE SUMMARY OF THE ANALYZED METHODS REGARDING THE MULTICLASS AND BINARY CHANGE DETECTION. VALUES IN PARENTHESIS ARE THE VARIANCE OF KAPPA.

	Multiclass – kappa		**Binary – F1-Score**		
	UTCM+MLC	UTCM+SVM	WECS	UTCM+MLC	UTCM+SVM
Area 1	0.754 (0.471×10^{-4})	0.685 (0.563×10^{-4})	0.824	0.977	0.963
Area 2	0.774 (0.744×10^{-4})	0.729 (0.854×10^{-4})	0.749	0.966	0.966

in the results obtained by the UTCM method. Moreover, one may observe that the MLC is most subject to map aperiodic changes compared to the SVM classifier.

Regarding computational cost, Figure 16 summarizes the run-time spent processing the experiments represented in Figures 8, 12 and 13. Naturally, the execution time increases in proportion to the image support. Furthermore, while the UTCM+MLC approach shows a very similar run-time independently of the parameters α_B and α_F, slight differences are observed when considering UTCM+SVM. This difference is assigned to the optimization process required to train the SVM. As expected, the computational complexity of UTCM surpasses that of WECS, with the latter exhibiting a maximum processing time of 24.6 seconds. This behavior is in agreement with the simpler WECS' algorithmic architecture, which is based on thresholding correlation values computed over the wavelet-smoothed image series.

V. CONCLUSIONS

This paper introduced a fully unsupervised data-driven framework for mapping landscape dynamics by integrating remote sensing image series, data transformation, statistical measures, and machine learning methods. Experiments with simulated and real-world remote sensing data were conducted to demonstrate the effectiveness and robustness of the designed framework.

Based on the presented results, it was verified that the proposed methodology, after a judicious parameter choice, was able to map targets according to three distinct profiles, namely periodic, aperiodic, and no change.

In contrast to most methods discussed in the literature, both classic and recent, our proposal not only allows distinguishing targets according to the three mentioned profiles but also offers an innovative way to extend unsupervised change detection from bi-temporal comparison to larger image series.

Notwithstanding, the proposed technique has limitations. The first limitation arises from the KL transformation, which may not be optimal for heavily skewed data. Nonetheless, this issue may be mitigated by adopting alternative decomposition techniques. Another limitation stands for the image series length, where a sufficient number of instants is required to compute the temporal dynamic representation (i.e., $\mathcal{W}$) and the partial autocorrelation values (i.e., $\mathcal{A}$).

As perspectives for future work, we include:

1) the analysis of other machine learning methods as a classifier model;
2) the evaluation of additional remote sensors, including hyperspectral instruments and aerial photos;
3) the adaptation of our methodology to distinguish further types of periodic and aperiodic changes;

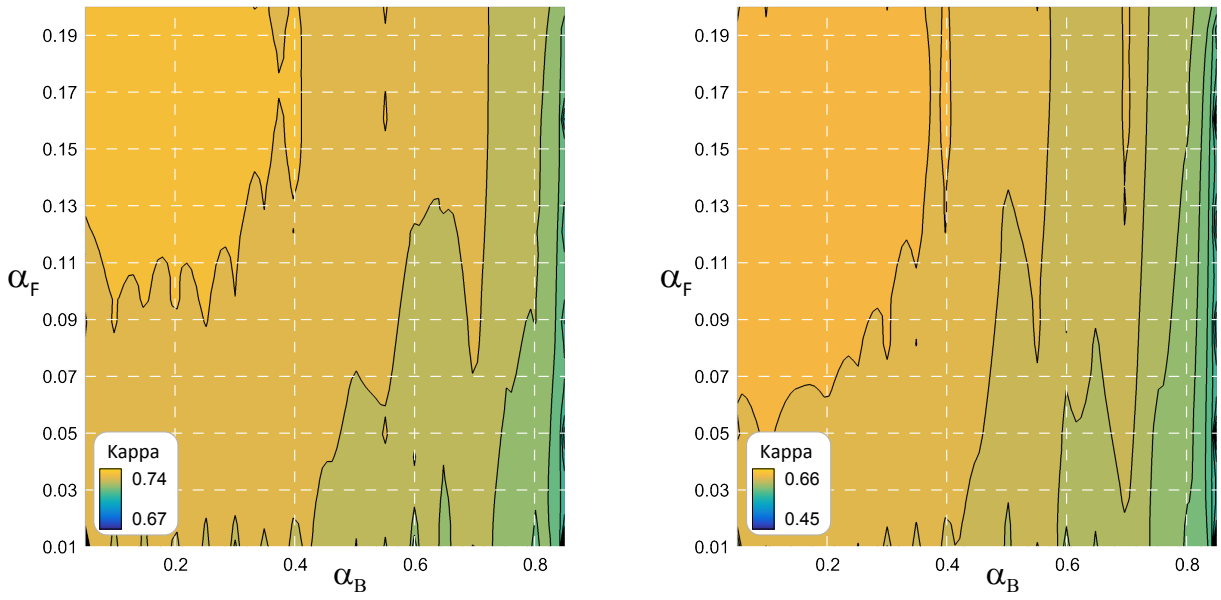

(a) UTCM+MLC (b) UTCM+SVM

Fig. 12. Performance on Area 1, in terms of the kappa coefficient, for distinct classification models and parameters α_B and α_F.

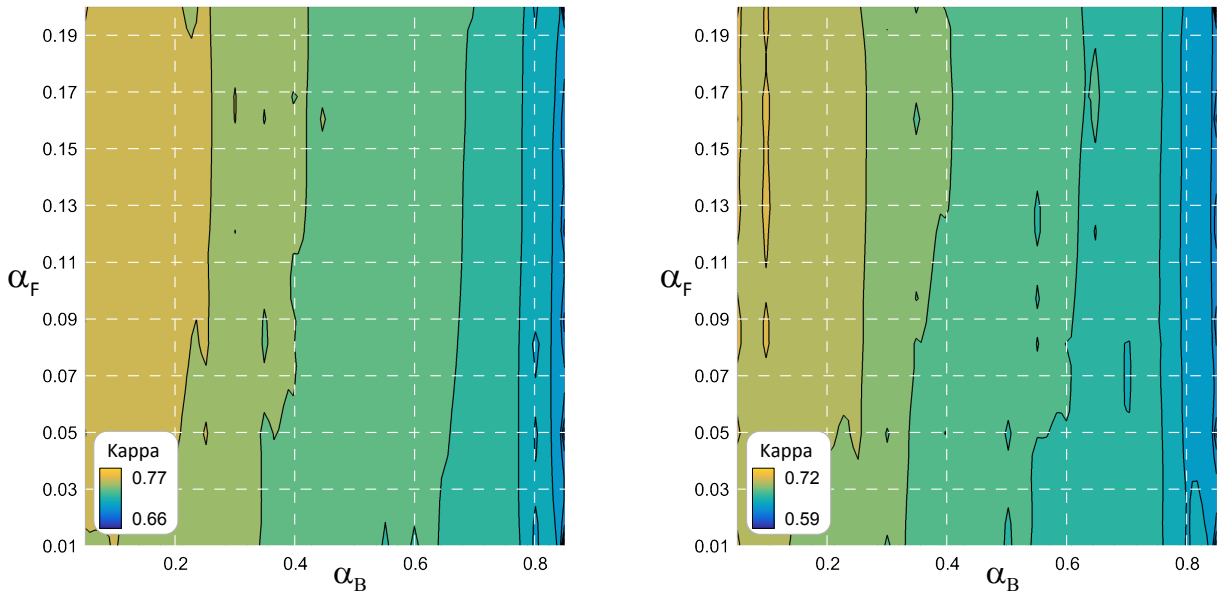

(a) UTCM+MLC (b) UTCM+SVM

Fig. 13. Performance on Area 2, in terms of the kappa coefficient, for distinct classification models and parameters α_B and α_F.

4) the development of an uncertainty representation in complement to the output results.

REFERENCES

[1] M. Hussain, D. Chen, A. Cheng, H. Wei, and D. Stanley, "Change detection from remotely sensed images: From pixel-based to object-based approaches," *ISPRS Journal of Photogrammetry and Remote Sensing*, vol. 80, pp. 91–106, 2013.

[2] L. Bruzzone and F. Bovolo, "A novel framework for the design of change-detection systems for very-high-resolution remote sensing images," *Proceedings of the IEEE*, vol. 101, no. 3, pp. 609–630, 2013.

[3] X. Lu, Y. Yuan, and X. Zheng, "Joint dictionary learning for multispectral change detection," *IEEE Transactions on Cybernetics*, vol. 47, no. 4, pp. 884–897, 2017.

[4] B. Du, L. Ru, C. Wu, and L. Zhang, "Unsupervised deep slow feature analysis for change detection in multi-temporal remote sensing images," *IEEE Transactions on Geoscience and Remote Sensing*, vol. 57, no. 12, pp. 9976–9992, 2019.

[5] C. Wu, B. Du, and L. Zhang, "Slow feature analysis for change detection in multispectral imagery," *IEEE Trans. Geosci. Remote Sens.*, vol. 52, no. 5, pp. 2858–2874, 2014.

[6] M. Volpi, D. Tuia, G. Camps-Valls, and M. Kanevski, "Unsupervised change detection with kernels," *IEEE Geoscience and Remote Sensing Letters*, vol. 9, no. 6, pp. 1026–1030, 2012.

[7] S. Liu, L. Bruzzone, F. Bovolo, M. Zanetti, and P. Du, "Sequen-

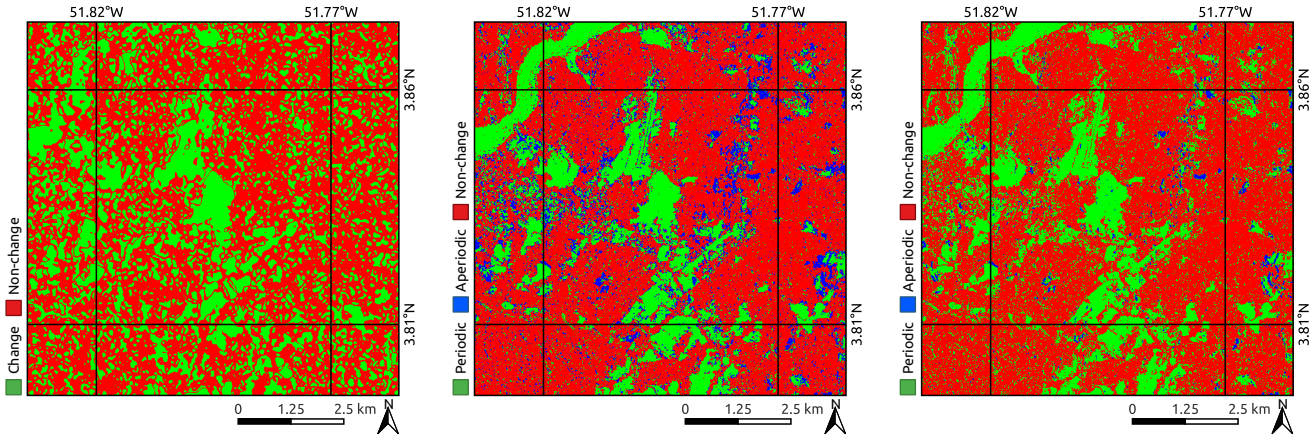

(a) WECS (Binary) (b) UTCM+MLC (c) UTCM+SVM

Fig. 14. Best result achieved on Area 1 by the proposed and alternative methods.

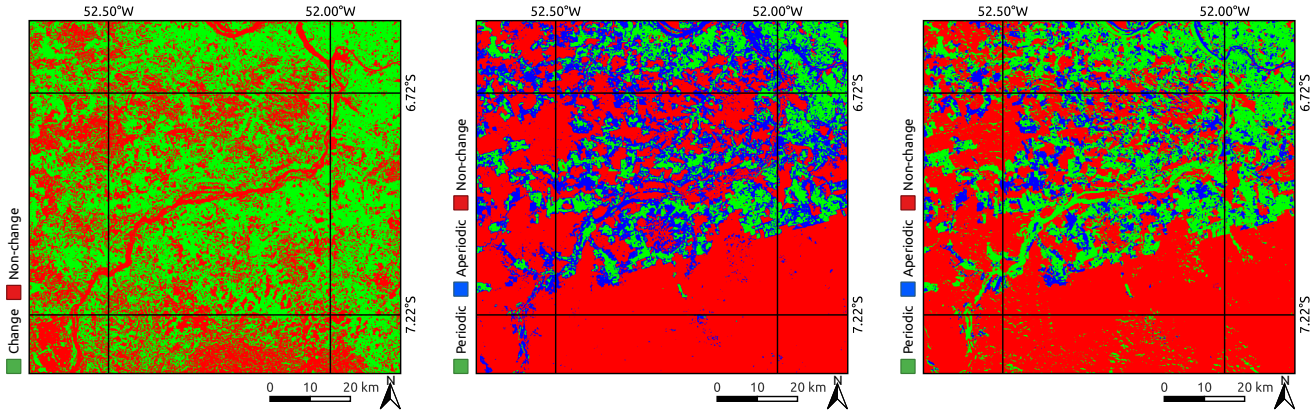

(a) WECS (Binary) (b) UTCM+MLC (c) UTCM+SVM

Fig. 15. Best result achieved on Area 2 by the proposed and alternative methods.

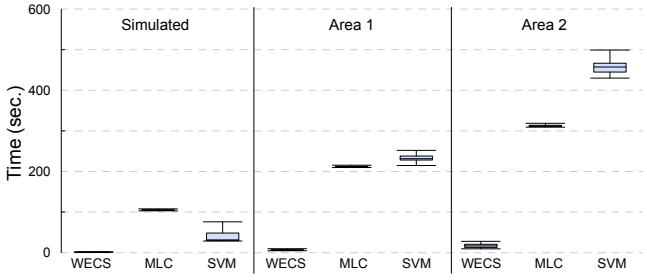

Fig. 16. Run-time of the alternative and proposed method using the MLC and SVM models as classifier.

tial spectral change vector analysis for iteratively discovering and detecting multiple changes in hyperspectral images," *IEEE Transactions on Geoscience and Remote Sensing*, vol. 53, no. 8, pp. 4363–4378, 2015.

[8] M. Hao, W. Shi, H. Zhang, and C. Li, "Unsupervised change detection with expectation-maximization-based level set," *IEEE Geoscience and Remote Sensing Letters*, vol. 11, no. 1, pp. 210–214, 2014.

[9] M. Gong, Y. Li, L. Jiao, M. Jia, and L. Su, "Sar change detection based on intensity and texture changes," *ISPRS Journal of Photogrammetry and Remote Sensing*, vol. 93, pp. 123–135, 2014.

[10] K. Conradsen, A. A. Nielsen, and H. Skriver, "Determining the points of change in time series of polarimetric sar data," *IEEE Transactions on Geoscience and Remote Sensing*, vol. 54, no. 5, pp. 3007–3024, 2016.

[11] A. D. C. Nascimento, A. C. Frery, and R. J. Cintra, "Detecting changes in fully polarimetric SAR imagery with statistical information theory," *IEEE Transactions on Geoscience and Remote Sensing*, vol. 57, no. 3, pp. 1380–1392, Mar 2019.

[12] M. Zanetti and L. Bruzzone, "A theoretical framework for change detection based on a compound multiclass statistical model of the difference image," *IEEE Transactions on Geoscience and Remote Sensing*, vol. 56, no. 2, pp. 1129–1143, 2018.

[13] P. Zhang, M. Gong, H. Zhang, J. Liu, and Y. Ban, "Unsupervised difference representation learning for detecting multiple types of changes in multitemporal remote sensing images," *IEEE Transactions on Geoscience and Remote Sensing*, vol. 57, no. 4, pp. 2277–2289, 2019.

[14] S. Chirakkal, F. Bovolo, A. R. Misra, L. Bruzzone, and A. Bhattacharya, "A general framework for change detection using multimodal remote sensing data," *IEEE Journal of Selected Topics in Applied Earth Observations and Remote Sensing*, vol. 14, pp. 10 665–10 680, 2021.

[15] R. V. Fonseca, R. G. Negri, A. Pinheiro, and A. M. Atto, "Wavelet spatio-temporal change detection on multitemporal sar images," *IEEE Journal of Selected Topics in Applied Earth*

Observations and Remote Sensing, vol. 16, pp. 4013–4023, 2023.
[16] H.-C. Li, T. Celik, N. Longbotham, and W. J. Emery, "Gabor feature based unsupervised change detection of multitemporal sar images based on two-level clustering," *IEEE Geoscience and Remote Sensing Letters*, vol. 12, no. 12, pp. 2458–2462, 2015.
[17] L. Huang, Y. Fang, X. Zuo, and X. Yu, "Automatic change detection method of multitemporal remote sensing images based on 2d-otsu algorithm improved by firefly algorithm," *Journal of Sensors*, 2015.
[18] D. Wen, X. Huang, L. Zhang, and J. A. Benediktsson, "A novel automatic change detection method for urban high-resolution remotely sensed imagery based on multiindex scene representation," *IEEE Transactions on Geoscience and Remote Sensing*, vol. 54, no. 1, pp. 609–625, 2016.
[19] D. Ratha, S. De, T. Celik, and A. Bhattacharya, "Change detection in polarimetric sar images using a geodesic distance between scattering mechanisms," *IEEE Geoscience and Remote Sensing Letters*, vol. 14, no. 7, pp. 1066–1070, 2017.
[20] C. Wu, L. Zhang, and B. Du, "Kernel slow feature analysis for scene change detection," *IEEE Transactions on Geoscience and Remote Sensing*, vol. 55, no. 4, pp. 2367–2384, 2017.
[21] Q. Ran, W. Li, and Q. Du, "Kernel one-class weighted sparse representation classification for change detection," *Remote Sensing Letters*, vol. 9, no. 6, pp. 597–606, 2018.
[22] L. T. Luppino, F. M. Bianchi, G. Moser, and S. N. Anfinsen, "Unsupervised image regression for heterogeneous change detection," *CoRR*, vol. abs/1909.05948, 2019. [Online]. Available: http://arxiv.org/abs/1909.05948
[23] S. Saha, F. Bovolo, and L. Bruzzone, "Unsupervised deep change vector analysis for multiple-change detection in vhr images," *IEEE Transactions on Geoscience and Remote Sensing*, vol. 57, no. 6, pp. 3677–3693, 2019.
[24] Y. Lin, S. Li, L. Fang, and P. Ghamisi, "Multispectral change detection with bilinear convolutional neural networks," *IEEE Geoscience and Remote Sensing Letters*, vol. 17, no. 10, pp. 1757–1761, 2020.
[25] P. Du, X. Wang, D. Chen, S. Liu, C. Lin, and Y. Meng, "An improved change detection approach using tri-temporal logic-verified change vector analysis," *ISPRS Journal of Photogrammetry and Remote Sensing*, vol. 161, pp. 278–293, 2020.
[26] S. Saha, F. Bovolo, and L. Bruzzone, "Building change detection in vhr sar images via unsupervised deep transcoding," *IEEE Transactions on Geoscience and Remote Sensing*, vol. 59, no. 3, pp. 1917–1929, 2021.
[27] D. Wang, X. Chen, M. Jiang, S. Du, B. Xu, and J. Wang, "Ads-net:an attention-based deeply supervised network for remote sensing image change detection," *International Journal of Applied Earth Observation and Geoinformation*, vol. 101, p. 102348, 2021.
[28] C. Wu, H. Chen, B. Du, and L. Zhang, "Unsupervised change detection in multitemporal vhr images based on deep kernel pca convolutional mapping network," *IEEE Transactions on Cybernetics*, vol. 52, no. 11, pp. 12 084–12 098, 2022.
[29] J. Shi, Z. Zhang, C. Tan, X. Liu, and Y. Lei, "Unsupervised multiple change detection in remote sensing images via generative representation learning network," *IEEE Geoscience and Remote Sensing Letters*, vol. 19, pp. 1–5, 2022.
[30] C. E. Shannon, "A mathematical theory of communication," *Bell System Technical Journal*, vol. 27, 1948.
[31] M. Salicru, D. Morales, M. Menendez, and L. Pardo, "On the applications of divergence type measures in testing statistical hypotheses," *Journal of Multivariate Analysis*, vol. 51, no. 2, pp. 372–391, 1994.
[32] A. C. Frery, A. D. C. Nascimento, and R. J. Cintra, "Analytic expressions for stochastic distances between relaxed Complex Wishart distributions," *IEEE Trans. Geoscience and Remote Sensing*, vol. 52, no. 2, pp. 1213–1226, 2014.
[33] L. Devroye, L. Györfi, and G. Lugosi, *A Probabilistic Theory of Pattern Recognition*, ser. Applications of Mathematics. New York: Springer-Verlag, 1996, no. 31.
[34] R. Gonzalez and R. Woods, *Digital Image Processing*. Pearson, 2018.
[35] R. G. Negri, A. C. Frery, W. Casaca, S. Azevedo, M. A. Dias, E. A. Silva, and E. H. Alcântara, "Spectral–spatial-aware unsupervised change detection with stochastic distances and support vector machines," *IEEE Transactions on Geoscience and Remote Sensing*, vol. 59, no. 4, pp. 2863–2876, 2021.
[36] R. G. Negri and A. C. Frery, "Unsupervised change detection driven by floating references: A pattern analysis approach," *Pattern Analysis and Applications*, vol. 24, no. 3, pp. 933–949, aug 2021.
[37] N. Otsu, "A threshold selection method from gray-level histograms," *IEEE Trans. on Systems, Man, and Cybernetics*, vol. 9, no. 1, pp. 62–66, 1979.
[38] J. Kittler and J. Illingworth, "Minimum error thresholding," *Pattern Recognit.*, vol. 19, no. 1, pp. 41–47, 1986.
[39] J. Devore, *Probability and Statistics for Engineering and the Sciences*, 9th ed. Cengage Learning, 2015.
[40] R. G. Congalton and K. Green, *Assessing the Accuracy of Remotely Sensed Data*. Boca Raton: CRC Press, 2009.
[41] C. J. van Rijsbergen, *Information retrieval*, 2nd ed. London: Butterworths, 1979. [Online]. Available: http://www.dcs.gla.ac.uk/Keith/Preface.html
[42] S. Theodoridis and K. Koutroumbas, *Pattern Recognition*, 4th ed. San Diego: Academic Press, 2008.
[43] A. R. Webb and K. D. Copsey, *Statistical Pattern Recognition*, 3rd ed. John Wiley & Sons, Ltd, 2011.

Rogério G. Negri received the graduated degree in Mathematics (2006) from São Paulo State University (UNESP), and the M.Sc. (2009) and Ph.D. (2013) in Applied Computation from Instituto Nacional de Pesquisas Espaciais (INPE). He is currently Associate Professor at UNESP, São José dos Campos and a CNPq Research Productivity Fellow. His main research interests include pattern recognition, machine learning, image processing and remote sensing.

Alejandro C. Frery (Senior Member, IEEE) received the B.Sc. degree in Electronic and Electrical Engineering from the Universidad de Mendoza, Argentina, in 1983, the M.Sc. degree in Applied Mathematics (Statistics) from the Instituto de Matemática Pura e Aplicada (IMPA), Rio de Janeiro, Brazil, in 1990, and the Ph.D. degree in Applied Computing from the Instituto Nacional de Pesquisas Espaciais (INPE), São José dos Campos, Brazil, in 1993. Since 2019, he has been a Huashan Scholar with the Key Laboratory of Intelligent Perception and Image Understanding of the Ministry of Education, Xidian University, Xi'an, China. He is also a statistics and data science Professor with the Victoria University of Wellington, Wellington, New Zealand. His research interests include statistical computing and stochastic modeling. Dr. Frery was the recipient of the 2018 IEEE Geoscience and Remote Sensing Society Regional Leader Award. He was the Editor-in-Chief of IEEE Geoscience and Remote Sensing Letters from 2014 to 2018, and he is currently the Vice-President for Publications of the IEEE Geoscience and Remote Sensing Society.

Wallace Casaca received the B.Sc. and M.Sc. degree in pure and applied mathematics from São Paulo State University (UNESP), Brazil, in 2008 and 2010, respectively, and the Ph.D. degree in computer sciences and applied mathematics from University of São Paulo (USP), Brazil, in 2014. During his doctoral studies, he worked as a visiting researcher at Brown University. He is currently a Professor with UNESP, São José do Rio Preto. He is a Research Associate at the CEPID-FAPESP Center for Research in Mathematical Sciences Applied to Industry (CeMEAI), and a CNPq Research Productivity Fellow. His research interests include computer vision, remote sensing, machine learning, visualization, computational intelligence, data science and numerical analysis.

Paolo Gamba (Fellow, IEEE) is Professor at the University of Pavia, Italy in the Telecommunications and Remote Sensing Laboratory. He received the Laurea degree in Electronic Engineering "cum laude" from the University of Pavia, Italy, in 1989, and the Ph.D. in Electronic Engineering from the same University in 1993. He served as Editor-in-Chief of the IEEE Geoscience and Remote Sensing Letters from 2009 to 2013, and as Chair of the Data Fusion Committee of the IEEE Geoscience and Remote Sensing Society (GRSS) from October 2005 to May 2009. He has been elected in the GRSS AdCom from 2014 to 2022, served as GRSS President from 2019 to 2020, and is currently the Editor-in-Chief of the IEEE Geoscience and Remote Sensing Magazine. He also served as Technical Co-Chair of the 2010, 2015 and 2020 IGARSS conferences, in Honolulu (Hawaii), Milan (Italy), and on-line, respectively. He is Fellow of IEEE, IAPR, AAIA and the Academia Europaea. He has been invited to give keynote lectures and tutorials on several occasions about urban remote sensing, data fusion, EO data for physical exposure and risk management. He published more than 190 papers in international peer-review journals.

Avik Bhattacharya (Senior Member, IEEE) received the integrated M.Sc. degree in Mathematics (M'08–SM'16) from the Indian Institute of Technology, Kharagpur, India, in 2000 and the Ph.D. degree in remote sensing image processing and analysis from Télécom ParisTech, Paris, France, and the Ariana Research Group, Institut National de Recherche en Informatique et en Automatique (INRIA), Sophia Antipolis, Nice, France, in 2007. He is a Professor at the Centre of Studies in Resources Engineering, Indian Institute of Technology Bombay (CSRE, IITB), Mumbai, India. Before joining IITB, he was a Canadian Government Research Fellow at the Canadian Centre for Remote Sensing (CCRS) in Ottawa, ON, Canada. He received the Natural Sciences and Engineering Research Council of Canada visiting scientist fellowship at the Canadian national laboratories from 2008 to 2011. His current research interests include SAR polarimetry, statistical analysis of polarimetric SAR images, and applications of Radar Remote Sensing in Agriculture, Cryosphere, Urban, and Planetary studies. Dr. was the Associate Editor and then the Editor-in-Chief of IEEE Geoscience and Remote Sensing Letters (GRSL) from 2019 to 2023. He has been the Guest Editor of the special issue on Applied Earth Observations and Remote Sensing in India in the IEEE Journal of Selected Topics in Applied Earth Observations and Remote Sensing (J-STARS), 2017. He was one of the guest editors of the special stream on Advanced Statistical Techniques in SAR Image Processing and Analysis in IEEE Geoscience and Remote Sensing Letters, 2018. He is the Founding Chairperson of the IEEE Geoscience and Remote Sensing Society (GRSS) Chapter of the Bombay Section. He leads the Microwave Remote Sensing Lab (www.mrslab.in) at CSRE, IITB.